Local probe comparison of ferroelectric switching event statistics in the creep and depinning regimes in $Pb(Zr_{0.2}Ti_{0.8})O_3$ thin films - Supplementary Information

Philippe Tückmantel[1], Iaroslav Gaponenko[1], Nirvana Caballero[1], Joshua A. Agar[2,3], Lane W. Martin[3], Thierry Giamarchi[1], and Patrycja Paruch[1]

[1]Department of Quantum Matter Physics, University of Geneva, Switzerland

[2]Department of Material Science and Engineering, Lehigh University, Bethlehem, Pennsylvania, USA

[3]Department of Material Science and Engineering, University of California, Berkeley, California, USA

[*]philippe.tueckmantel@unige.ch

1 Brief review of creep and depinning of elastic interfaces in disordered media

In the framework of disordered elastic systems, the main ingredients affecting the interface geometry are its elasticity, which tends to favor a flat line configuration (or plane depending on the interface dimensionality) and the disorder, which pins the interface and promotes meandering. Additionally, an externally applied force will drive the overall movement of the interface through the disordered medium. The system displays glassy physics as the energy landscape exhibits many local minima and the interface wanders through consecutive metastable states. The competition between these a priori simple ingredients leads to the rich physics of avalanches and scale-invariance of event size and energy distributions.

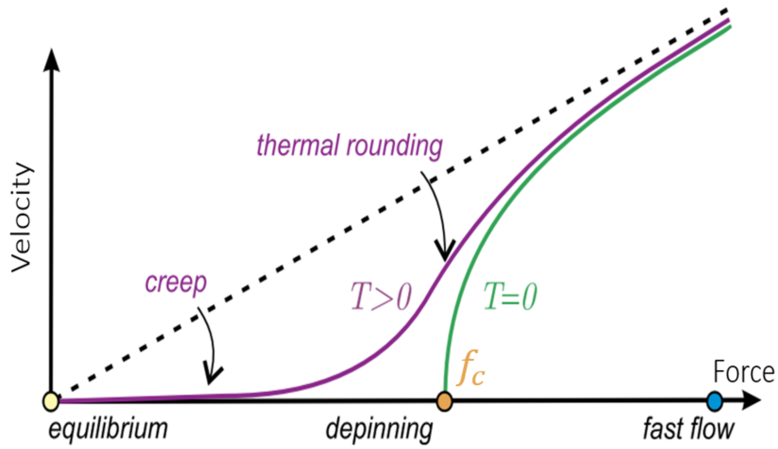

Figure 1. Velocity-force curve in disordered elastic systems theory at $T = 0$ (green) and $T > 0$ (purple). At $T = 0$, the interface is pinned in place until a critical force f_c above which it is depinned. At finite temperature, motion of the interface occurs through thermal activation. Adapted from[1]

The velocity-force curve of a propagating domain wall is shown in Fig. 1. At zero temperature, the interface remains pinned with no observable motion below a critical value f_c of the external force f. As the external force is increased through f_c, the interface is depinned, and its global velocity exhibits a power-law dependence on the driving force $v \sim (f - f_c)^{\beta}$, where β is a universal exponent. The depinning process as the system crosses f_c can thus be seen as a second order dynamic phase transition with the velocity as an order parameter and the external force as the conjugate field. At sufficiently high forces above depinning $f >> f_c$, the interface presents a linear response to the driving force. At finite temperature, the system can also be excited thermally, and thus presents ultraslow dynamics even below f_c. In this so-called creep regime, the interface velocity follows a stretched exponential behavior $v \sim exp(-\beta U_c(\frac{f}{f_c})^{\mu})$, where $\beta = 1/K_bT$, U_c is the characteristic height of the potential energy barriers the interface needs to overcome, and the creep exponent μ depends on the universality class of the disorder and on the dimensionality of the interface. Thermal activation also leads to a characteristic rounding of the depinning transition.

Around $f = f_c$, the motion of the interface occurs in a wide range of event sizes and with a power-law distribution $P(S) \sim S^{-\tau} f_S(S/S_c)$, where f_S is a size cutoff function, which decays sharply as $S > S_c$ and is a constant for $S < S_c$. S_c is a characteristic event size which depends on the external force, the dimensionality of the interface and its static roughness. In ferroelectric and ferromagnetic systems, the event size S refers to the surface spanned by individual switching events, as measured in magnetic systems either directly via magneto-optic Kerr microscopy[2–4] or indirectly by inductive techniques[5] and measured indirectly in ferroelectrics through acoustic noise measurements[6]. For a 1-dimensional interface in random bond disorder, commonly observed in ferroelectrics, the size exponents in the creep regime is expected to be $4/5$,[7] while in the depinning regime, the exponent is expected to be higher, at ~ 1.11[8]. More recent theoretical work focusing on the dynamics of elastic interfaces deep in the creep regime also show spatio-temporal clustering of the switching events, as well as a crossover of size exponents above a critical size[9]. The exact exponents of the power-law scaling of event sizes and detailed picture of the creep regime are therefore still under debate. For more information on disordered elastic systems theory, detailed descriptions of the creep regime and crackling characteristic size exponents the reader is invited to turn to[10–14], while more information on crackling phenomena in a more general context can be found in[15,16].

2 Event size extraction

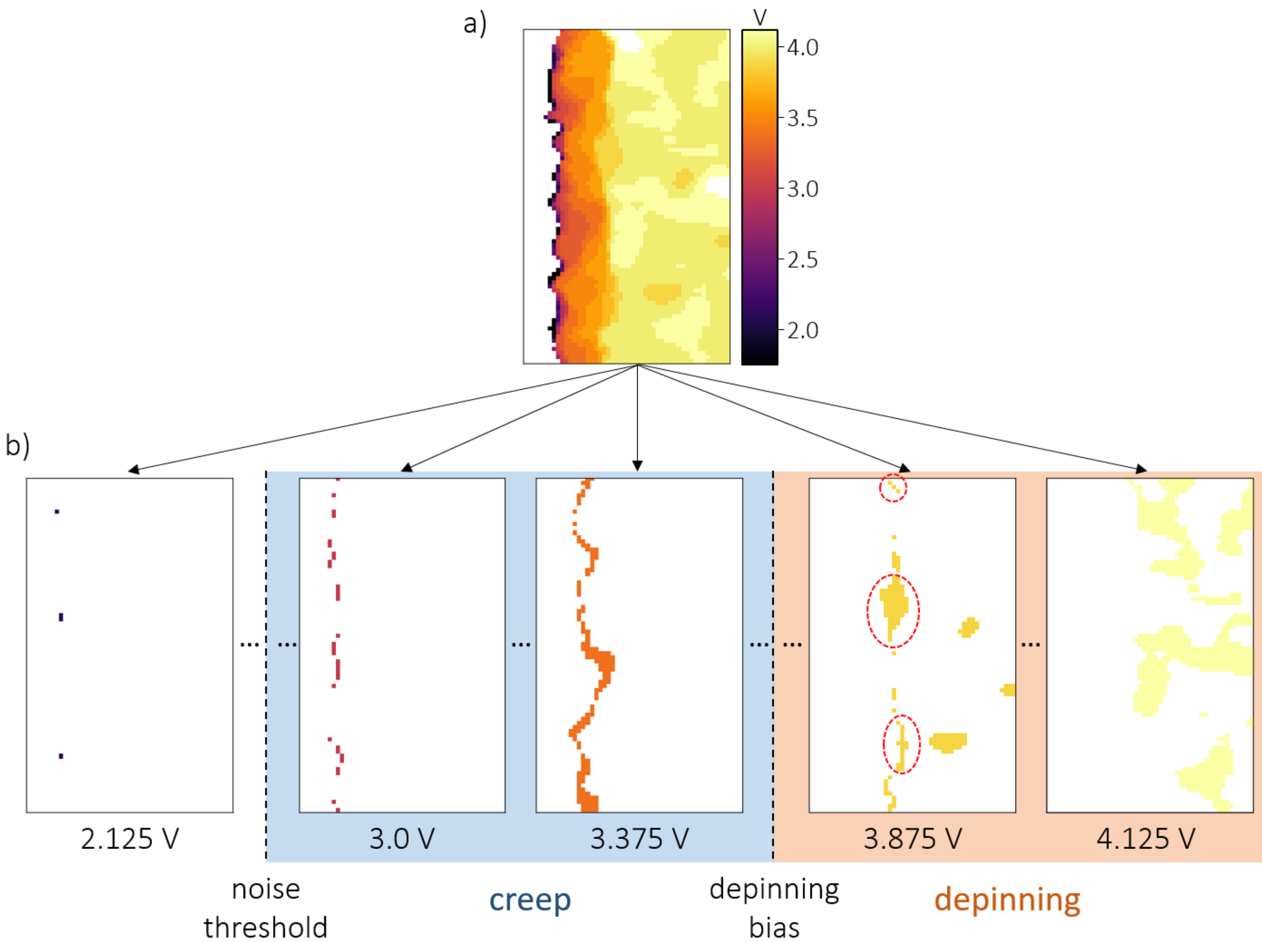

Figure 2. Schematic representation of the event sizes extraction process. (a) Cumulative map of switching events color coded as the bias at which each event occurred. (b) Snapshots of polarization reversal events occurring at various tip voltages. Some examples of separate events, whose size can be computed from the number of pixels comprising the event, are highlighted with dashed red lines. Using the techniques described in the main text, the creep and depinning regimes can be identified and the distribution of event sizes extracted for particular dynamic regimes.

The measurements consisted of scans at a fixed sub-coercive DC bias gradually switching the polarization, alternated with PFM scans in order to image the domain configuration after each switching scan. The DC bias of the i^{th} scan V_i was kept constant throughout the switching scan but was increased from one switching scan to the next by a fixed interval ΔV of 125 mV in PZT-Nuc and 100 mV in PZT-Mot. The polarization reversal events triggered during each switching scan can be mapped from the differences of the binarized successive PFM images acquired after each scan, as shown in Fig. 2(a), where the color-coding corresponds to the tip bias at which each event took place. These are the maps shown in figure 1(b-e) of the main text. The switching events occurring at each tip bias are extracted as illustrated in Fig. 2b, and their size can be computed in terms of their surface on the image by counting the number of pixels making up each event. Some examples of separate events are surrounded with a dashed red line. Once the noise threshold and the depinning bias are known, the voltage window over which switching events are included can be restricted. In the main text, the distributions of events sizes are extracted first only in the creep regime, then in both the creep and depinning regimes.

3 Sample characterization

The samples used in this study are thin films of $Pb(Zr_{0.2}Ti_{0.8})O_3$, grown on $SrTiO_3$ substrates, with a $SrRuO_3$ back electrode. PZT-Nuc and PZT-Mot samples were grown by off-axis RF magnetron sputtering and pulsed laser deposition, respectively. Both samples are 60–70 nm thick and show similar surface roughnesses of 0.3 and 0.4 nm for PZT-Nuc and PZT-Mot, respectively, but with quite different surface morphologies (Figure 3(a,b)). As shown in Figure 3 (c,d), XRD $2\theta/\omega$ scans along the (001) crystalline axis show a similar *c*-axis parameter of 4.14 Å for PZT-Nuc and 4.18 Å for PZT-Mot. Reciprocal space maps (Figure 3(e,f)) show that PZT-Nuc has relaxed with an *a*-axis parameter of 3.95 Å, while PZT-Mot is still mostly strained to the substrate with an a-axis of 3.905 Å, though some shift of the weight of the peak towards higher *a*-axis values can be observed, suggesting partial relaxation. The surface morphology and X-ray diffraction data are consistent with dislocations forming during growth as a result of sample-substrate mismatch strain, and altering the local adatom binding energy, resulting in a growth mode transition from step-flow to 3D nanoscale islands oriented along the crystalline axes[17]. Wavelength dispersion spectroscopy on both samples and analysis of the Pb/Zr ratios suggest that PZT-Mot has a slightly higher Pb content than PZT-Nuc with ratios of 5.6±0.8 and 8.5±2 respectively.

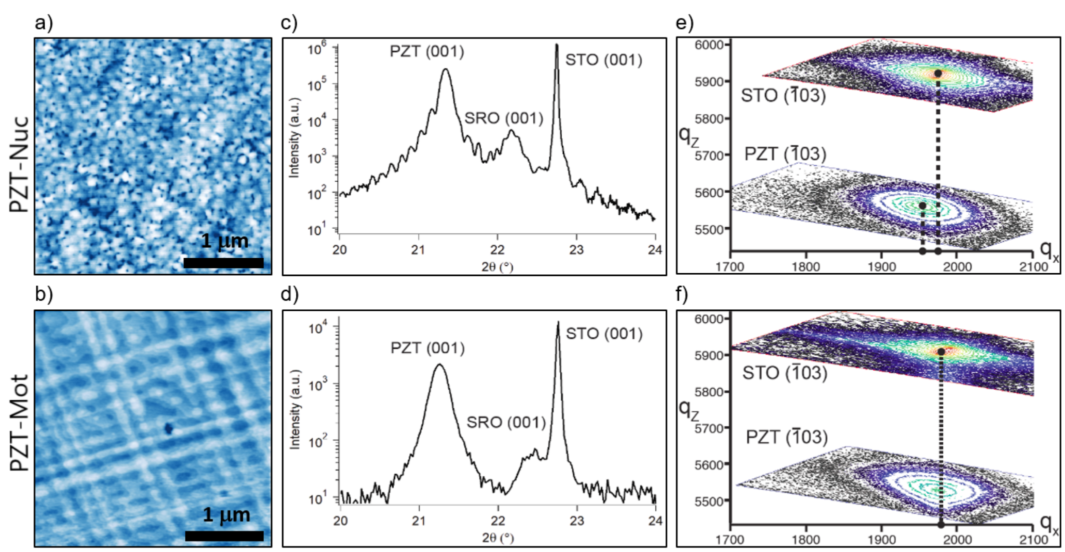

Figure 3. Characterization of the PZT-Nuc and PZT-Mot samples. (a,b) surface topography, (c,d) $2\theta/\omega$ scans along the *c*-axis, aligned on the (001) $SrTiO_3$ peak. (e,f) Reciprocal space map taken around (-103) showing in-plane relaxation in PZT-Nuc, while PZT-Mot is mostly strained to the substrate.

4 Differences in switching dynamics

In this section, the striking differences in polarization switching between PZT-Nuc and PZT-Mot are discussed in more detail. For PZT-Nuc, polarization reversal proceeds predominantly by the nucleation and growth of new domains, with relatively little motion of the pre-existing walls of the initial domain configuration. This is particularly noticeable under negative tip bias (Figure 1(b) in the main text), where the two side walls of the down-oriented central stripe domain move inwards by only 20 nm between -1.0 V and -1.5 V. Beyond this threshold, multiple new up-oriented domains nucleate in the central region and grow rapidly outwards, gradually merging until almost complete polarization reversal at -4 V. Under positive tip bias, we observe significantly higher activation thresholds for polarization switching, both via domain wall motion, which sets in at 3 V and contributes to somewhat larger 100 nm inward displacements of the existing domain walls, and subsequently via point nucleation and very rapid growth of new domains beyond 3.75 V leading to almost complete polarization reversal. For PZT-Mot, meanwhile, polarization reversal under both positive and negative tip bias proceeds almost exclusively via the motion of pre-existing domain walls (Figure 1(d,e) in the main text). These walls, initially relatively flat, begin moving via small displacements of around 25 nm at close to ±1 V. For negative tip bias, the motion appears quite regular and generalized to the entire domain walls, while for positive tip bias the displacements remain extremely limited until approximately 2.3 V is reached, at which point large jumps can be observed, leading to complete polarization reversal. Under negative tip bias, the domain walls also appear to roughen more noticeably while they move.

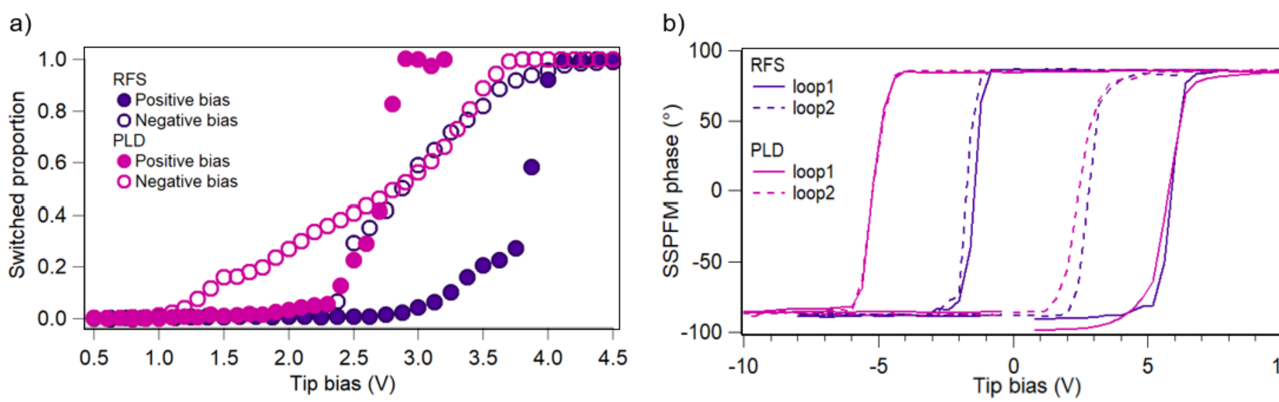

Figure 4. (a) Normalized switching rates in PZT-Nuc and PZT-Mot, showing earlier onset of switching at negative bias, but more rapid full polarization reversal at positive bias, as well as changes in switching rates corresponding to the onset of rapid domain nucleation and merging. (b) SSPFM loops averaged over 25 locations showing bias history dependence of the positive branch of the coercive tip bias.

The effect of domain-writing history on the overall switching behavior can be seen from the evolution of the normalized switched surface, calculated as the ratio of the switched area to the total area in which the polarization is initially oriented opposite to the applied electric field, as shown in Fig. 4(a). In both samples, onset of domain wall motion occurs at a higher bias when switching from the as-grown polarization state with positive bias, as could be expected given the inherent asymmetry of the device configuration, as previously reported in numerous ferroelectric thin films under writing by an atomic force microscope tip[18–20]. The switched surface proportion first increases slowly close to the onset of switching, then much more rapidly at higher bias. At negative bias, corresponding to switching domains previously written with high tip bias of 8 V and 10 V in PZT-Mot and PZT-Nuc respectively, the switching is much more gradual. In these regions, new defects and defect redistribution resulting from the writing are expected to provide additional pinning of the domain walls. In all cases, the switching rates clearly show a difference between a relatively limited regime of domain wall motion at lower positive bias, and then more rapid switching, whether by further domain wall motion or nucleation and growth of new domains at higher bias values.

To understand the differences we observe in switching behavior at positive and negative bias, we also need to consider the effects of switching history. As mentioned in the main text, the intense, localized, and highly inhomogeneous electric field applied by an SPM tip during writing has been shown to redistribute, inject and modify defects[21–25]. Thus, switching with a positive voltage (up to down) is carried out in the as-grown state of the sample, with an annealed equilibrium defect landscape established during film growth and cooling, while negative voltage switching (down to up) is carried out in areas previously switched with a 8 - 10 V bias, which we presume to modify the disorder potential landscape, possibly promoting both higher nucleation rates and stronger pinning.

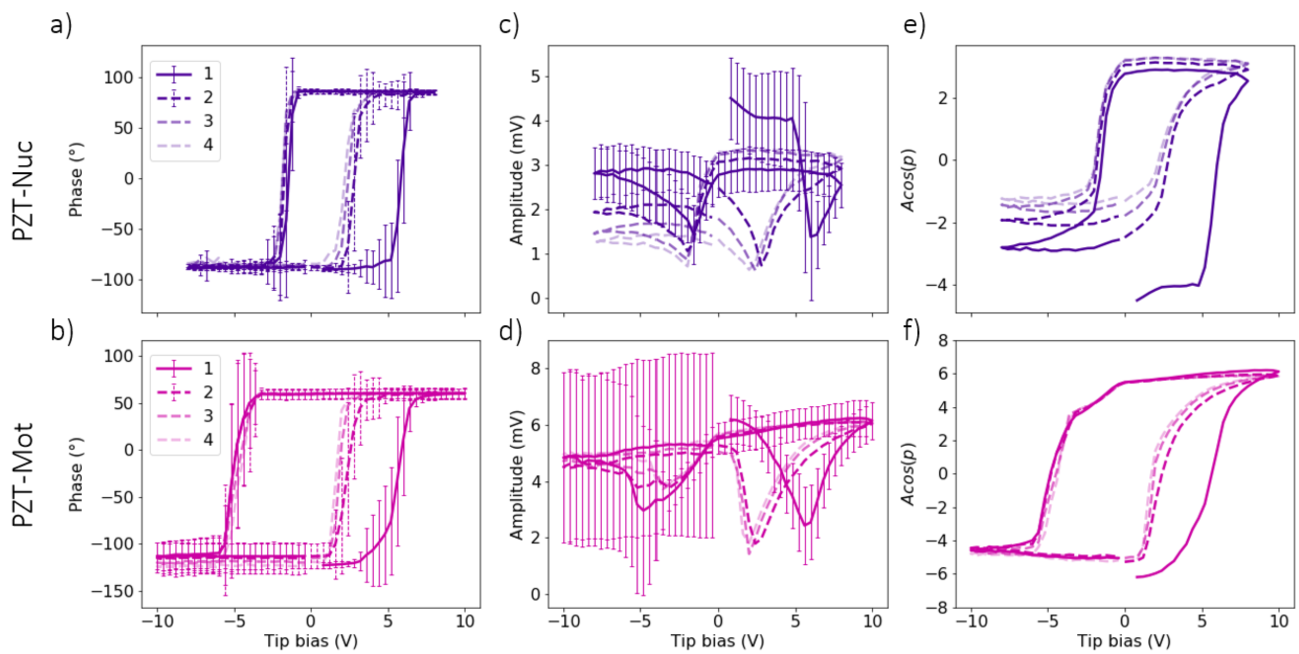

Figure 5. SSPFM phase and amplitude signals averaged over a 5x5 point grid and mixed signal calculated for PZT-Nuc (a,c,e) and PZT-Mot (b,d,e). The error bars at each point are calculated as the standard deviation of the measured signal value over the 25 points. The error bars are shown for the first two loops in the phase signal and for the first loop in the amplitude for visibility.

The influence of domain writing history is further observed in the differences between the first and second local hysteresis loops, acquired by switching spectroscopy PFM[26] (SSPFM) and shown in Fig. 4(b). Consecutive SSPFM loops were acquired over 25 locations on both PZT-Mot and PZT-Nuc. The measured signals were averaged separately for each loop. The average

SSPFM phase for the first and second loops are displayed in Fig. 4(b) without error bars for visual clarity. Figure 5(a,b) shows all four phase loops for PZT-Nuc and PZT-Mot respectively, including the error bars for the first two loops (comparable to the error on the subsequent loops), estimated as the standard deviations across the 25 locations.

The first switching hysteresis loop from the as-grown P_{up} state shows an inherent asymmetry in PZT-Nuc with positive imprint suggesting that switching with $V_{tip} < 0$ (P_{down} to P_{up}) should be easier, as would be expected from the monodomain as-grown P_{up} state. After the first switching cycle however, the second hysteresis loop appears more symmetric, with lower coercive bias, especially on the positive branch, and the built-in field appears to be reduced. In contrast, the first hysteresis loop in PZT-Nuc is symmetric, but with relatively high coercive voltage, while after the first switching cycle the second hysteresis loop becomes more asymmetric, with switching appearing to be easier with a subsequent positive bias (P_{up} to P_{down}). The corresponding SSPFM amplitude loops are shown in figure 5(c,d), with the error bars included only for the first loop for visual clarity. The changes in coercive bias observed in the phase signals are visible in the amplitude as well, through changes in the bias value of the amplitude minima between the first and second loop. Although significant variations are observed across the 25 locations, resulting in large error bars, the amplitude signals shift in magnitude from one loop to the next, especially in PZT-Nuc, where the negative bias branch shows significant decrease, while the amplitude remains somewhat more stable in PZT-Mot after the first loop. The SSPFM phase and amplitude was used to calculate the mixed signal response $Rcos(\theta)$ with R and θ, the amplitude and phase signals respectively, and displayed in figure 5(e,f). The changes in coercive bias between the first and second loop are once again visible, as well as changes in the slope of the curves indicating possible changes in the switching process caused by defects injected or redistributed by the locally high electric field applied by the tip. While in PZT-Mot, loops 2-4 show only very small changes, the mixed signal loops in PZT-Nuc exhibit a consistent decrease in the saturation of the mixed signal at negative tip bias and a consistently reduced hysteresis area, possibly as a consequence of defect-induced softening of the polarization. These differences also confirm the presence of very different disorder landscapes in the two samples

The strong asymmetry as a function of polarity can also be seen from the maps showing the respective contribution of nucleation of new domains and motion and merging of existing domains, shown in Fig. 7. Specifically focusing on PZT-Nuc, the number of nucleation sites varies significantly, with 106 observed when switching the down-polarized areas (Fig. 7(a)), and only 20 when switching the up-polarized areas (Figure 2(b)). In addition, under negative bias nucleation initiates early and occurs over a much broader voltage range, suggesting a distribution of local activation thresholds, while under positive bias we observe a relatively narrow nucleation range, and the greatest contribution to polarization reversal is from the very rapid growth and merging of these newly formed domains, which appear much more mobile. In PZT-Mot, in contrast, no nucleation sites are observed at negative bias and only two at positive bias, suggesting much higher nucleation thresholds, consistent with an overall lower defect density.

5 Contribution of nucleation, motion and merging

The individual switching events can be categorized into domain nucleation and domain wall motion and merging using the connectivity of the newly switched areas with their surrounding areas that are already in the favored polarization orientation. The process is summarized in Fig. 6. The PFM phase signals are first binarized as schematically illustrated in Fig. 6(a,b). The pixel by pixel difference between consecutive binarized phase images is computed (6(c)), highlighting the newly switched areas. For each separate newly switched area, a count is made of the number of disconnected neighboring regions that were already switched. If that count is 0, then the newly switched area is an island of the favored polarization that is completely surrounded with a yet unswitched zone. The switching event therefore corresponds to the nucleation of a new domain. This is the case of region 1 in Fig 6(c). A count of 1 means that only one continuous region was touching the newly switched zone, and the switching event then corresponded to a motion of a single already existing domain. This is the case for regions 2 and 3 in Fig. 6(c). If the count is of 2 or more, then the newly switched area merged together two or more separate domains and the event is therefore categorized as merging, as is the case of region 4 in Fig. 6(c). This process yields the switching event map shown in Fig. 6(d).

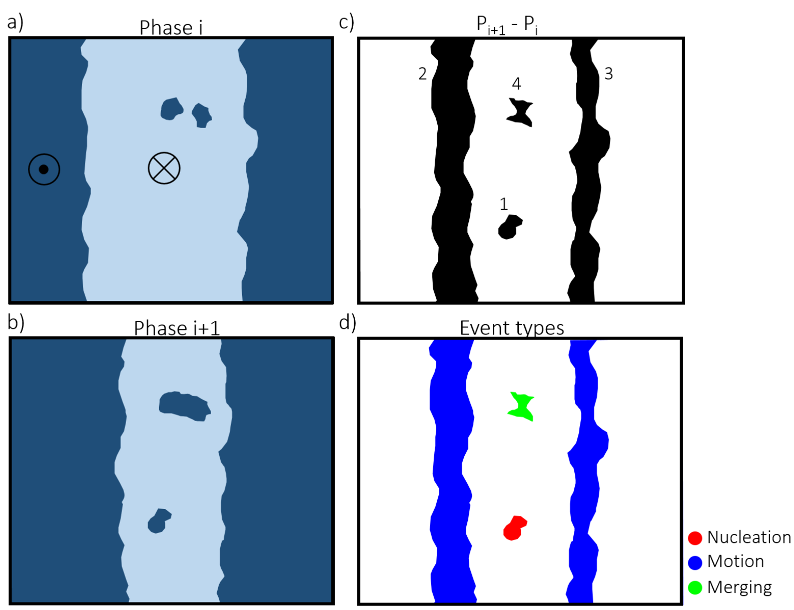

Figure 6. Workflow for identifying domain nucleation, motion and merging events. (a,b) Schematic consecutive binarized phase images. (c) Pixel by pixel difference between panels (b) and (a), highlighting in black the polarization reversal events occurring in (b). Areas where the polarization reversed are shown in black. (d) Nucleation, motion and merging events are identified for each newly switched events by counting the number separate regions neighboring regions that were already switched in (a). Regions with counts of 0, 1, >1 correspond to nucleation, motion and merging events respectively.

This technique applied to the data presented in the main text gives the cumulative maps of event types shown in Fig. 7. These maps highlight the much higher prevalence of nucleation events in PZT-Nuc (Fig. 7(a,b)) compared to PZT-Mot (Fig. 7(c,d)).

In the analysis presented in the main text, nucleation events are excluded from the size-distributions as their sizes are expected to be determined by the critical nucleus[27], and only domain wall motion and merging are considered. While the ability to discriminate between event types should allow the size-distributions to be extracted separately for these two types of events, exploring potential variations in their power-law scaling exponents, the present measurements do not provide sufficient statistics to warrant their separate treatment.

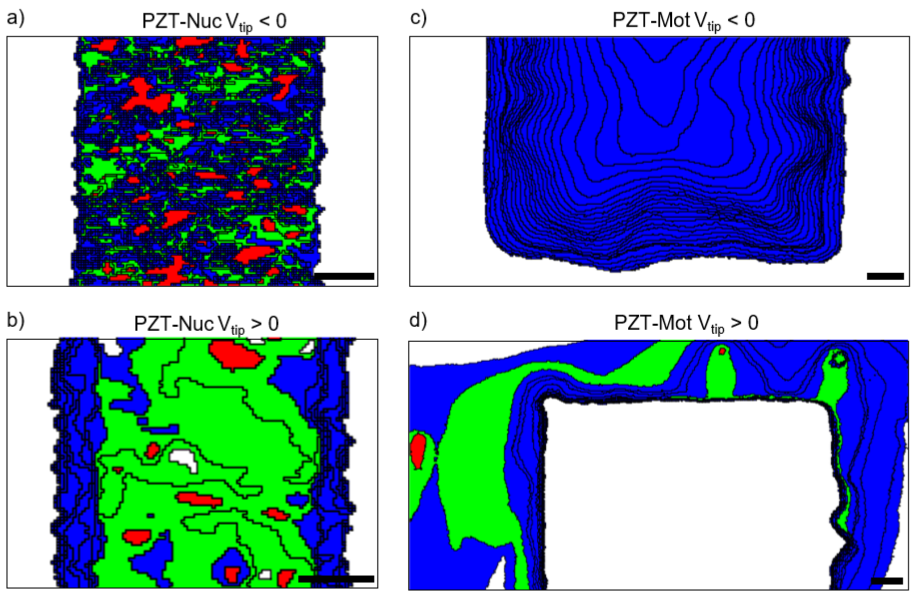

Figure 7. Maps showing different types of switching events - domain nucleation (red), domain wall motion (blue) and domain merging (green) - in the PZT-Nuc (a,b) and PZT-Mot (c,d) samples at negative and positive tip bias, respectively. The scalebars are 200 nm.

6 Estimation of noise thresholds

The overall domain displacements were used to estimate the range of tip voltages to be included in the power law fitting. To this end, the equivalent disc radius (EDR) of the domain wall displacement triggered during each switching scan was calculated. The EDR is shown for both samples and voltage polarities on a linear scale in Fig. 2 of the main text. The onset of domain displacement, which defines our lower cutoff is more clearly visible on a logarithmic scale, shown in Fig. 8. In the case of PZT-Nuc $V_{tip} < 0$ shown in panel (a), the same voltage window was chosen as for PZT-Nuc $V_{tip} > 0$ as discussed in the main text. In the case of PZT-Mot in panel (c), the noise threshold was chosen at a higher value of 2.3 V in order to avoid including the region between 1.5-2.2 V. In this region, the displacement is irregular due to tip surface contaminants temporarily adhering to the tip and altering the effective field applied to the film.

7 Lower bound estimate to the depinning bias

As mentioned in the main text, the method used to extract an estimate of the depinning bias is by construction an underestimate. This is especially true if the driving force is acquired over a restricted window as can be seen in Fig. 9. The dashed red rectangle

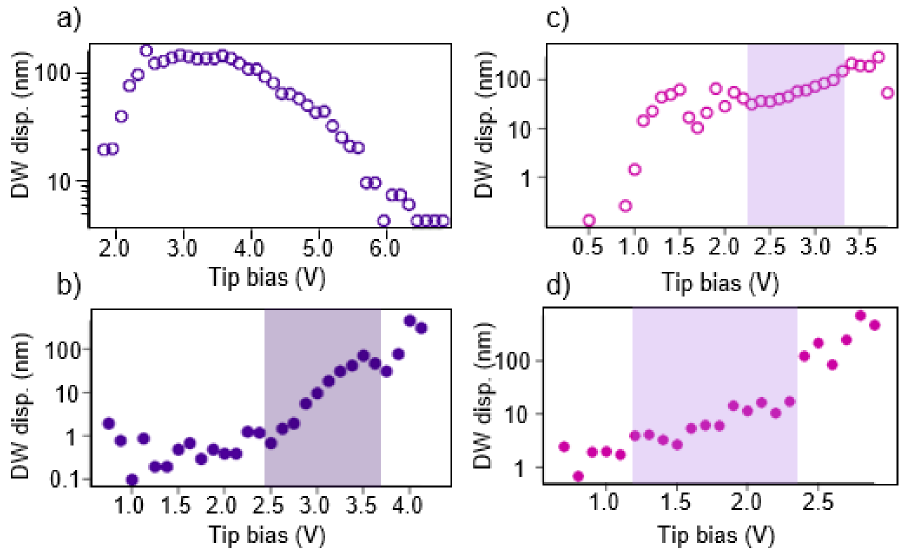

Figure 8. Equivalent disc radius of the overall domain displacement shown in a logarithmic scale for (a,b) PZT-Nuc $V_{tip} < 0$ and $V_{tip} < 0$ and (c,d) PZT-Mot $V_{tip} < 0$ and $V_{tip} < 0$. The shaded areas represent the range ov tip bias in which events were included in the creep regime.

represents the velocity-force curve extracted when the range of forces is limited and the linear flow regime is inaccessible. The resulting estimate of the depinning bias, extracted as the intercept to the line of highest displacements underestimates the critical force.

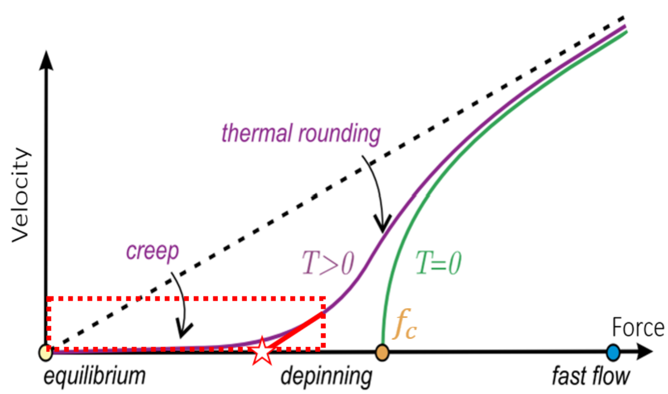

Figure 9. Interface velocity as a function of driving force in elastic models. Example of estimated depinning force when the range of applied forces is restricted. Adapted from[1].

8 Power law fitting

The power law fitting was performed using the maximum-likelihood method and the Powerlaw Python package[28], following the methods described by Clauset et al[29].

8.1 Procedure

At low event sizes, power law behavior is not expected to hold as a result of noise in the PFM images. To determine the cutoff values of the event sizes, we use the method described by Clauset et al[29], whereby a power law fitting is performed for all values of the cutoff (X_{min}). For each of these fits, the Kolmogorov-Smirnov (KS) distance is calculated between the cumulative distribution function (CDF) of the fit and the data. The chosen X_{min} corresponds to the value that minimises this KS distance. However, in some instances multiple values of X_{min} can yield very close KS distances. Each of these X_{min} values corresponds to different number of points taken into account in the fits: the lower the X_{min}, the more points are included in the analysis. Therefore, when the KS distances are very close, the lowest X_{min} among these values is chosen.

8.2 Boxing

The measurements on PZT-Mot with $V_{tip} < 0$ shows single switching events spanning the whole length of the domain wall. However, we know based on past studies of domain growth under a stationary biased tip[30] that the actual switching events must necessarily be local, given the effective dwell time which can be estimated based on the speed of the scanning tip during writing ($\sim$ 1-10 ms per pixel during a line scan).

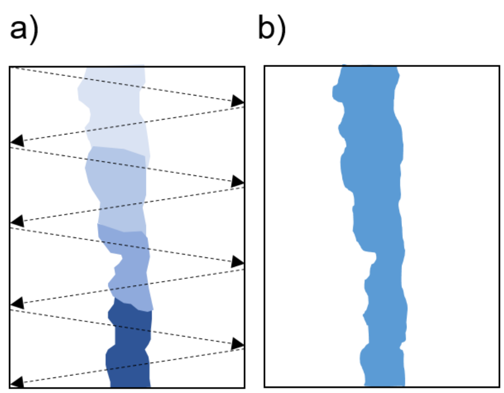

Figure 10. (a) Schematic of single switching events triggered by each passage of the biased AFM tip during a switching scans. (b) The interconnected switching events of panel (a) look like a single switching event in the subsequent PFM image taken after the switching scan. (c) Such behavior is seen in PZT-Mot, here at $V_{tip} < 0$.

That these switching events appear to coalesce into a single domain wall motion event as illustrated in Fig.10 is a consequence of scanning the entire area with a DC bias before performing a PFM imaging scan. However, this approach leads to very large apparent event sizes and very low statistics. In order to extract meaningful size exponents in this case, the domain wall areas were split into boxes as shown in Figure 11.

Here, we show this procedure with the dataset from PZT-Nuc $V_{tip} > 0$ measurements, as this allows a direct comparison of the exponent resulting from the boxing and from the standard power law fitting, providing validation of the technique. Event sizes were acquired for each box. To avoid correlations between adjacent boxes, the events for all the even and odd boxes were combined into two corresponding single distributions of events and fitted separately. The box width is also an important parameter. Narrow boxes lead to a higher number of events when the data from all the boxes are combined, but also limit the

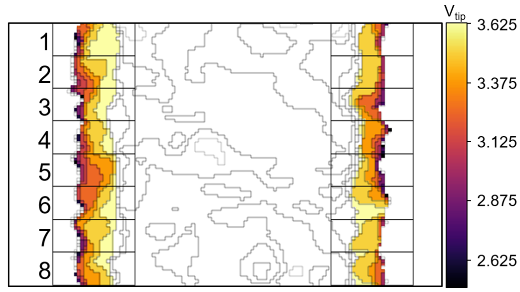

Figure 11. Example of boxing scheme. The switching events taken into account are color-coded according to the tip bias at which they occurred.

possible event sizes within the boxes. Wide boxes mean fewer total events taken into account in the fitting. Therefore, fits were performed for box widths between 1 and 40 pixels (7.81-312 nm). To analyse such a high number of fits rapidly and consistently, and to take into account the case of close KS values mentioned earlier, for each box size, the X_{min} values were split into 10 intervals as shown in Figure 12.

Within each interval, a fit was performed to determine X_{min} as the smallest KS, leading to 10 fits each for even and odd boxes. Figure 13 shows the resulting exponents, number of points and CDF of the data and corresponding fit for a box width of 10 pixels (78 nm). The thicker marker corresponds to the best overall fit. This procedure was repeated for all box sizes and for even and odd boxes. All the fit parameters (the optimal X_{min} within the interval, σ; the estimated error on τ, N) were recorded. Fits were eliminated by filtering out the ones with $\sigma > 0.5$, small box widths (typically 7-15 px or 55-120 nm) and high X_{min} values (typically around 150 nm^2. The final exponent attributed to the measurement corresponds to the average τ of the fits that passed the filtering process.

Figure 14 shows the exponent values and error estimates for the fits before and after filtering. The filtered fits have an average exponent of $\tau = 1.94 \pm 0.12$, compatible with the exponents obtained without boxing on this series ($\tau = 1.98 \pm 0.09$), thus validating the boxing procedure in the instances where it is the only statistically viable approach.

8.3 Results

8.3.1 Without bias cutoffs

The following figures (Figure 15 – Figure 18) show details of the power law fits for each of the measurement series when no cutoff in the tip bias is applied. The vertical dashed lines show the algorithmically chosen X_{min} value. The panels on the left show the KS distance, power law exponent τ and corresponding error estimate as a function of the X_{min} value. The panels on the right show the CDF and probability distribution function (PDF) for the data and the corresponding fits, as well as the associated exponent τ values, the estimated error, the number of events taken into account in the fit, and the chosen X_{min} value.

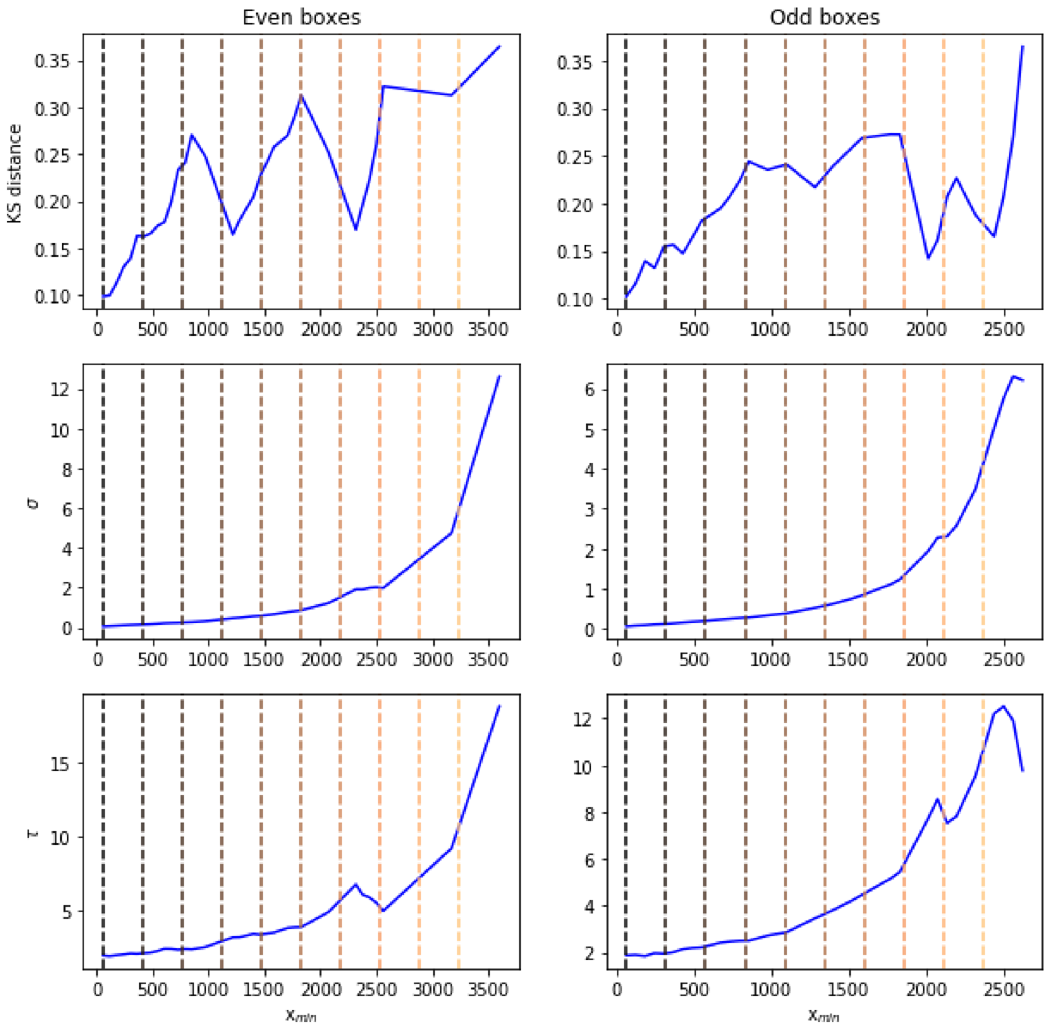

Figure 12. Kolmogorov-Smirnov (KS) distance, standard error and fitting exponent as a function of the size cutoff X_{min}. The dashed lines indicate the local fitting intervals.

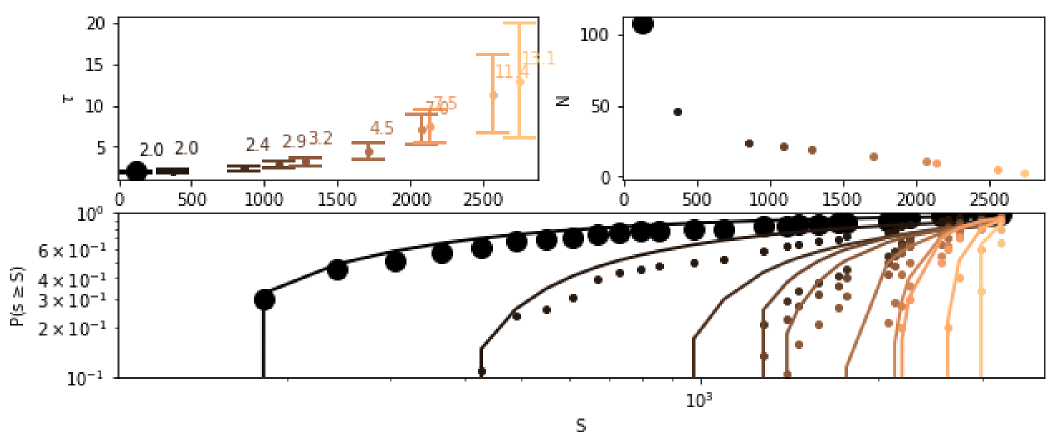

Figure 13. Fitting exponents, number of points taken into account in the fits, and probability distribution function (PDF) for each of the fit. The data is shown with circular markers and the fits with lines. The colors correspond to the fitting intervals in Figure 12

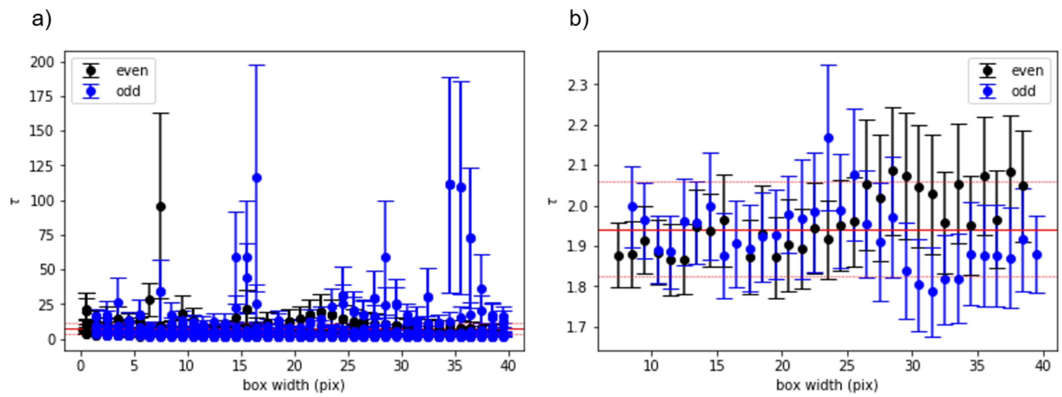

Figure 14. (a) Exponents for all boxing fits with no selection applied. (b) Exponents after filtering out the fits with $\sigma > 0.5$, box widths smaller than 55 nm and X_{min} higher than 245 nm^2.

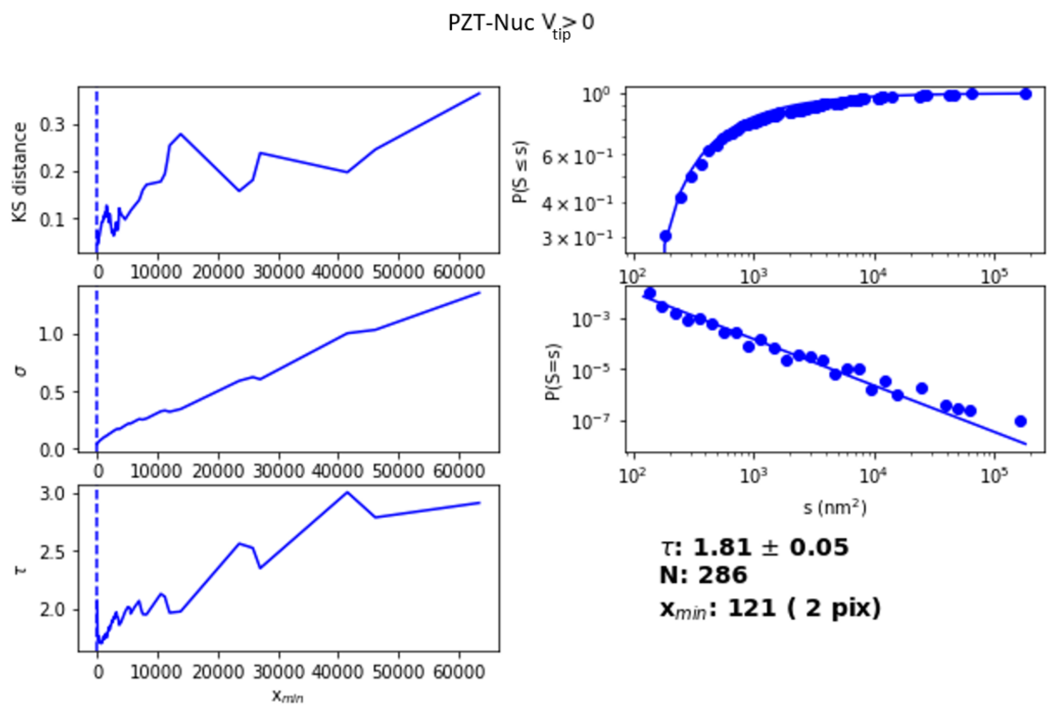

Figure 15. Power law fit characterization for the event sizes in PZT-Nuc with increasing positive tip bias. The blue dashed line shows the selected X_{min} value.

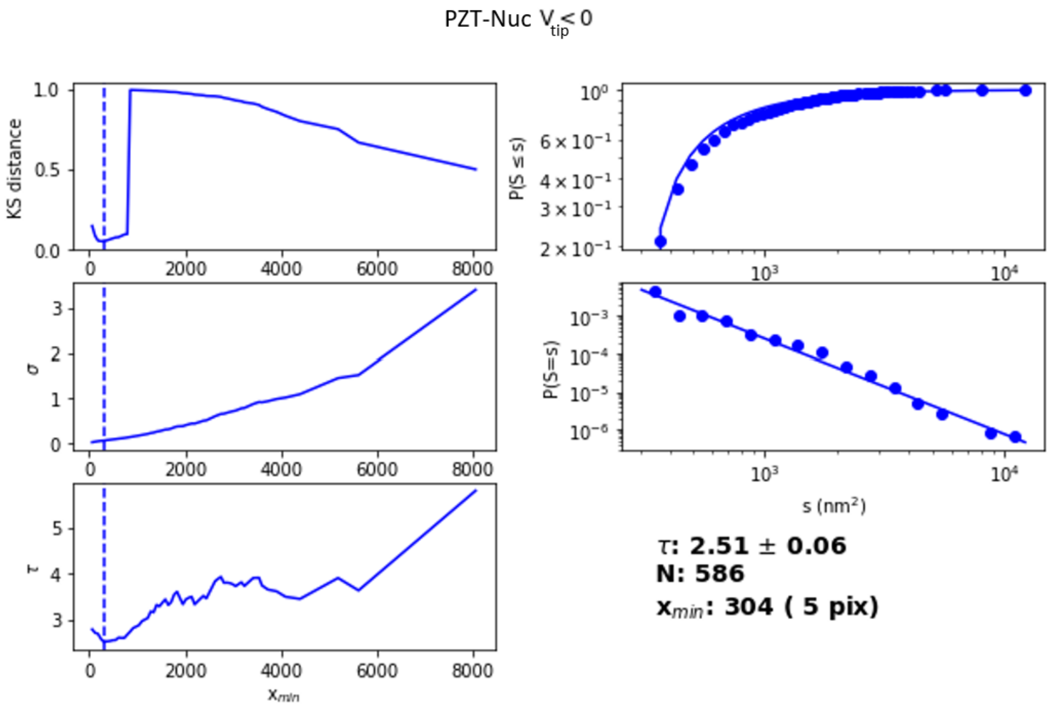

Figure 16. Power law fit characterization for the event sizes in PZT-Nuc with increasing negative tip bias. The blue dashed line shows the selected X_{min} value.

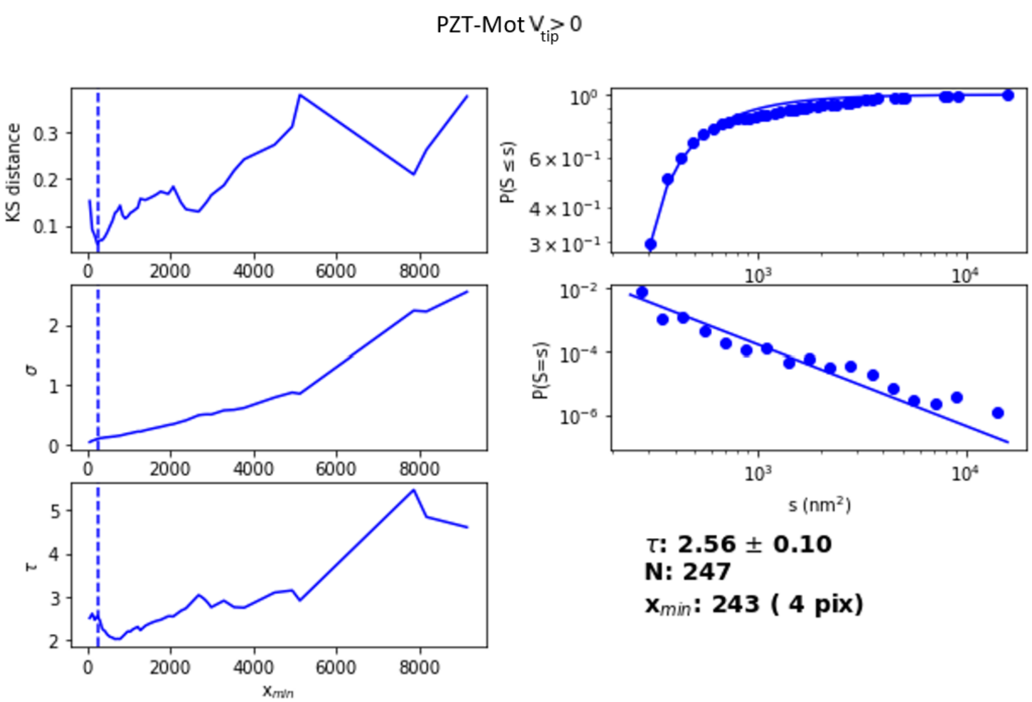

Figure 17. Power law fit characterization for the event sizes in PZT-Mot with increasing positive tip bias. The blue dashed line shows the selected X_{min} value.

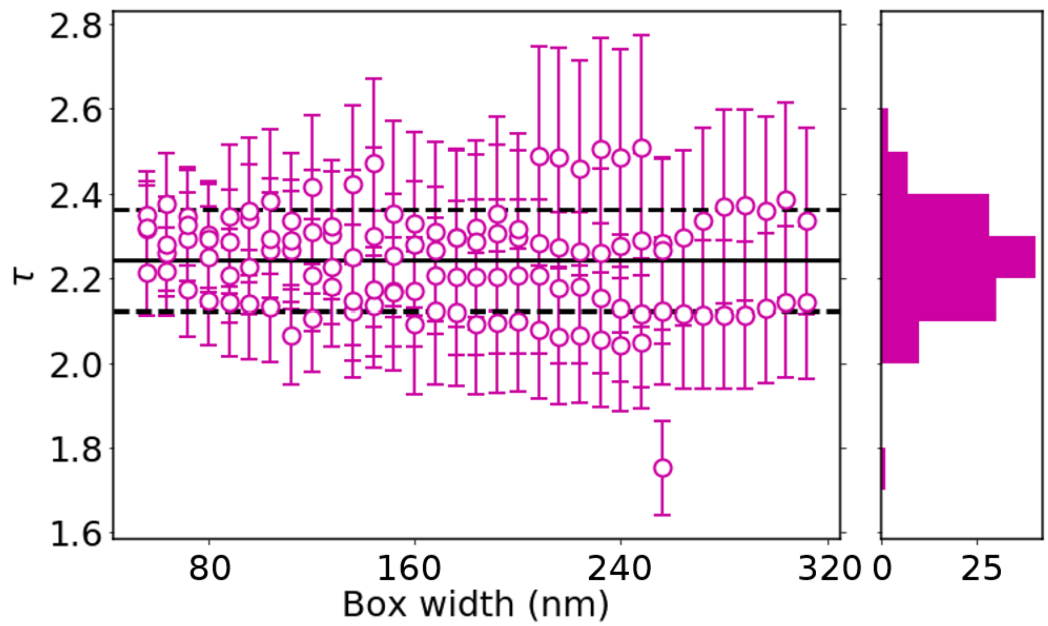

Figure 18. PZT-Mot V_{tip} <0. Filtered fits using the boxing technique described previously. The average exponent is 2.24 ± 0.17.

8.3.2 With bias cutoffs

In this section, we show for each measurement series the map of events within the applied bias cutoffs and the corresponding fits, similarly to the previous section. The vertical dashed lines show the algorithmically chosen X_{min} value. The panels on the left show the KS distance, power law exponent τ and corresponding error estimate as a function of the X_{min} value. The panels on the right show the CDF and probability distribution function (PDF) for the data and the corresponding fits, as well as the associated exponent τ values, the estimated error, the number of events taken into account in the fit, and the chosen X_{min} value. We also show the maps of events taken into account in the fitting. The included events occur in the voltage window between onset of domain wall movement up to our estimate of the depinning bias, as described in the main text. The grey lines show the outlines of switching events not included in the power law fitting.

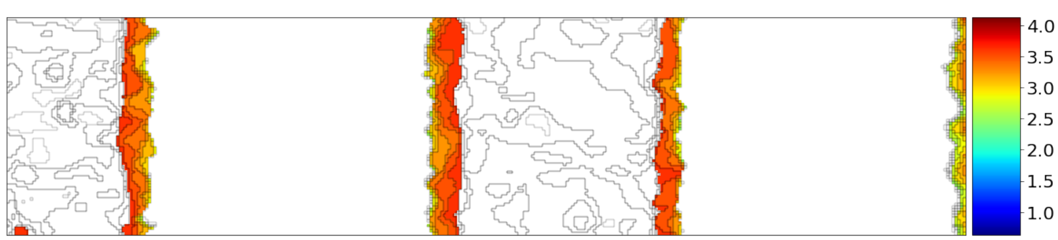

Figure 19. Events taken into account in the switching event size fits in PZT-Nuc with increasing positive tip bias. The grey lines show the outlines of switching events not included in the power law fitting.

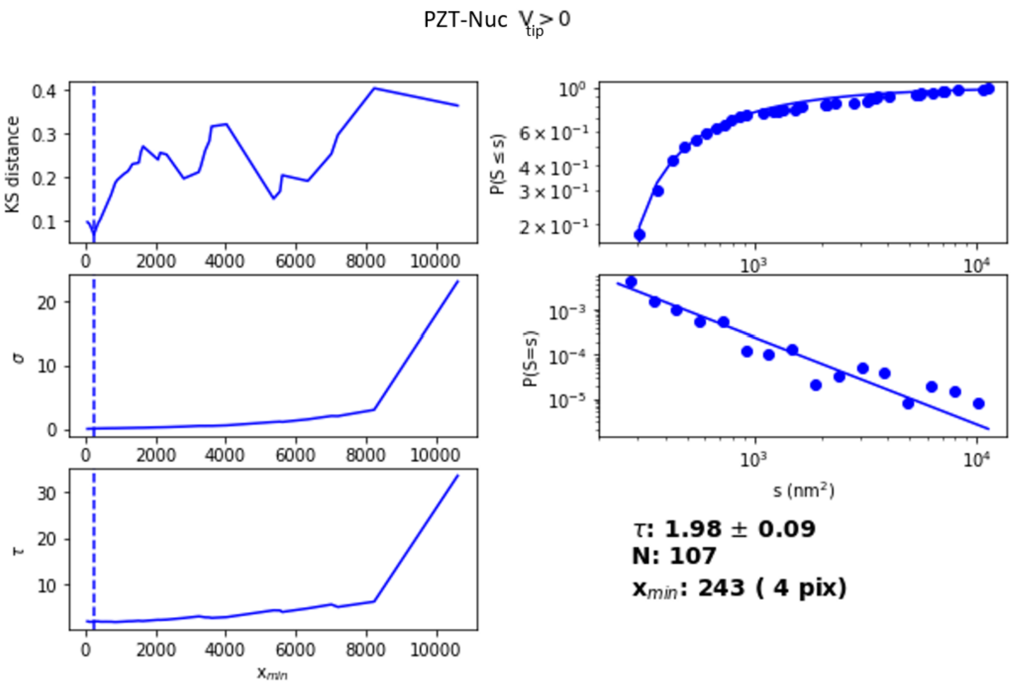

Figure 20. Power law fit characterization for the event sizes in PZT-Nuc with increasing positive tip bias. The blue dashed line shows the selected X_{min} value.

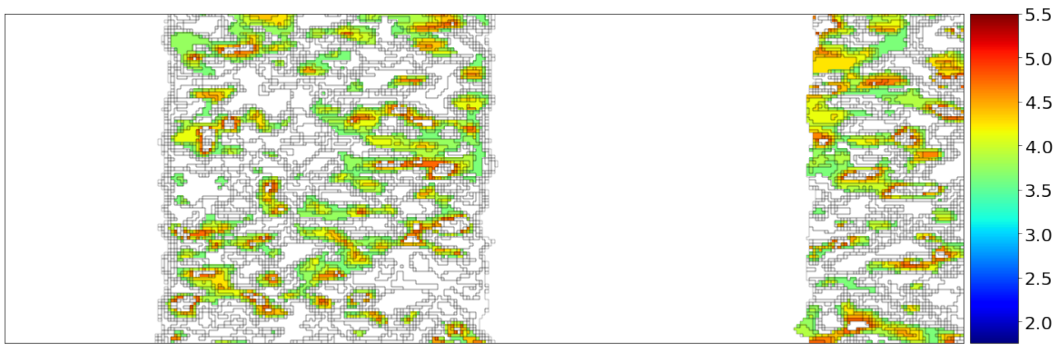

Figure 21. Events taken into account in the switching event size fits in PZT-Nuc with increasing negative tip bias. The grey lines show the outlines of switching events not included in the power law fitting.

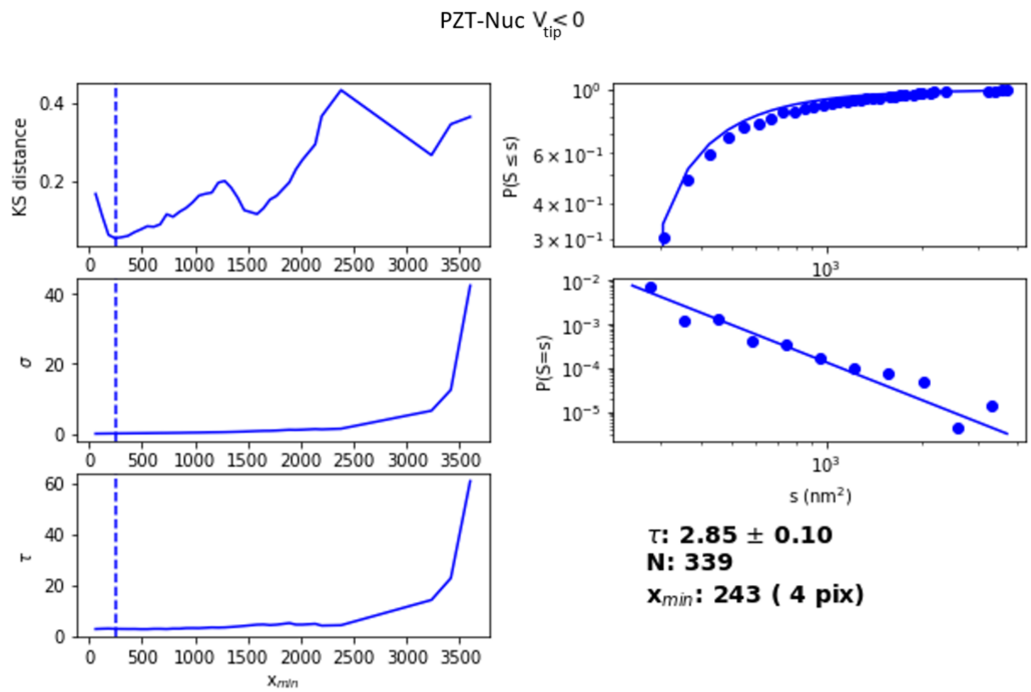

Figure 22. Power law fit characterization for the event sizes in PZT-Nuc with increasing negative tip bias. The blue dashed line shows the selected X_{min} value.

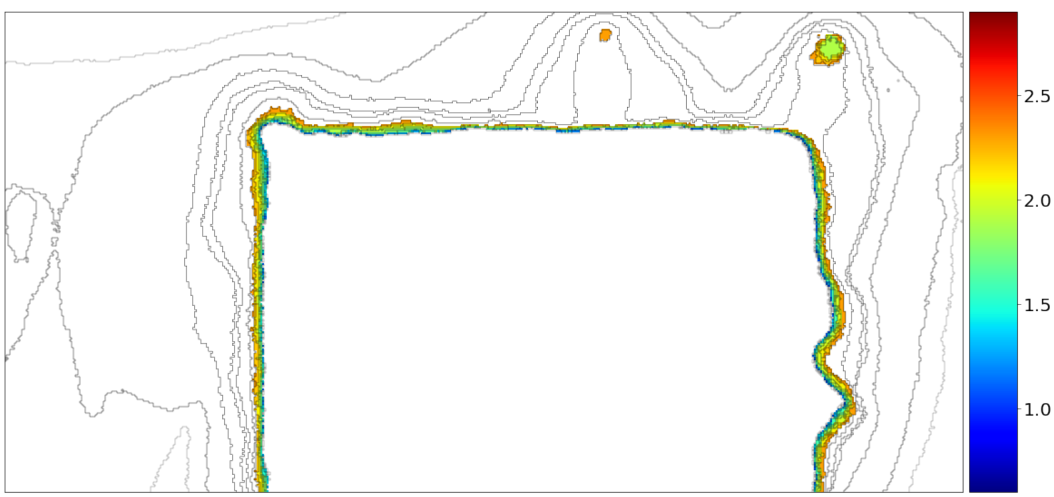

Figure 23. Events taken into account in the switching event size fits in PZT-Mot with increasing positive tip bias. The grey lines show the outlines of switching events not included in the power law fitting.

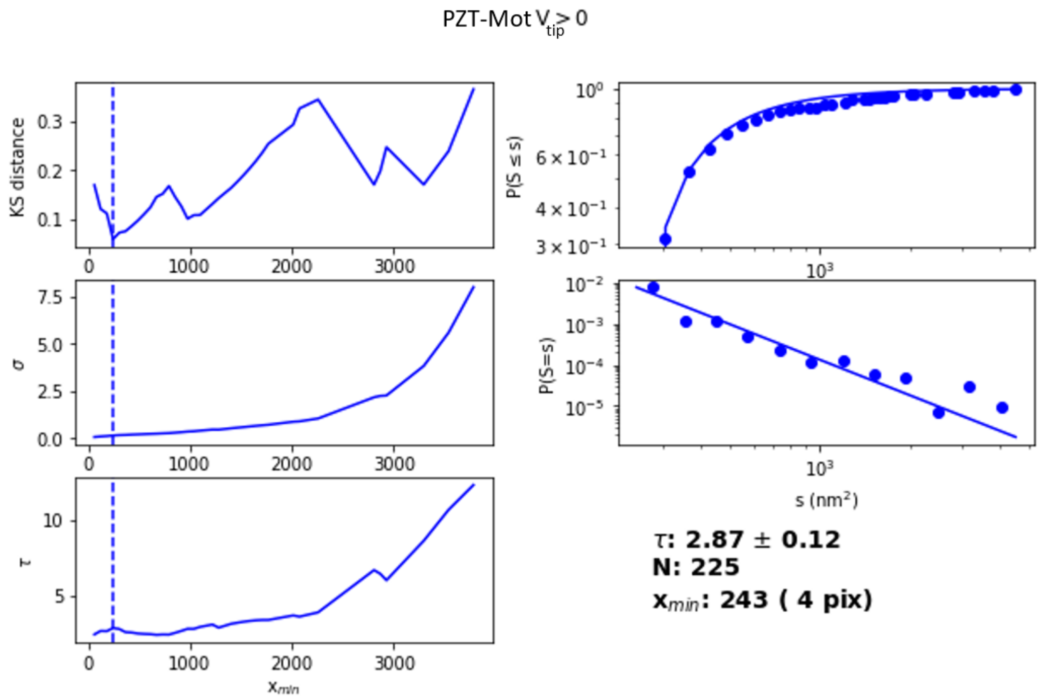

Figure 24. Power law fit characterization for the event sizes in PZT-Mot with increasing positive tip bias. The blue dashed line shows the selected X_{min} value.

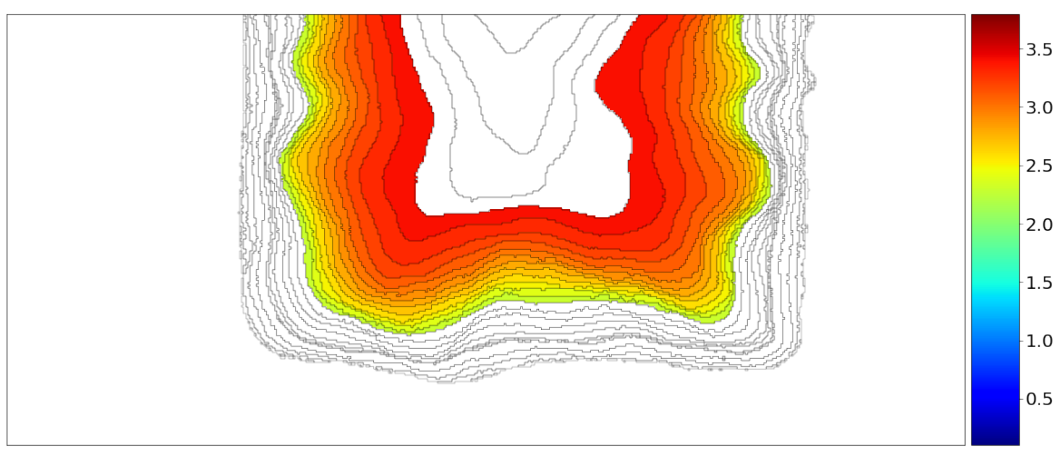

Figure 25. Events taken into account in the switching event size fits in PZT-Mot with increasing negative tip bias. The grey lines show the outlines of switching events not included in the power law fitting.

8.3.3 Constant switching bias

Here we show the details of the power law fits to the event sizes in the measurement series where the switching bias is kept constant.

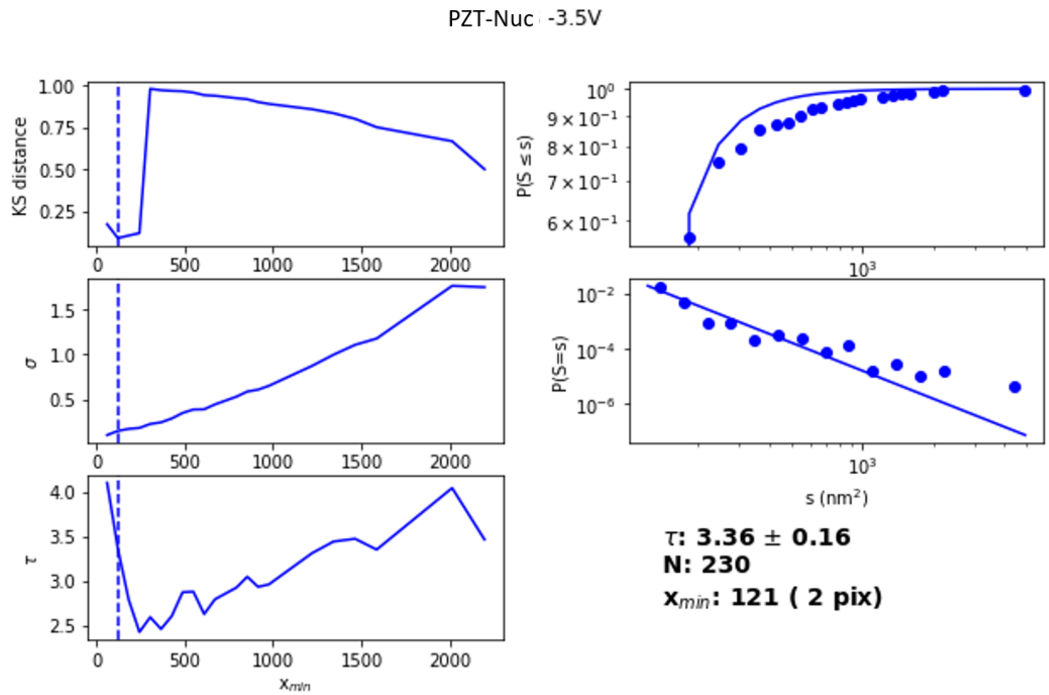

Figure 26. Power law fit characterization for the event sizes in PZT-Nuc with a constant tip bias of -3.5 V. The blue dashed line shows the selected X_{min} value.

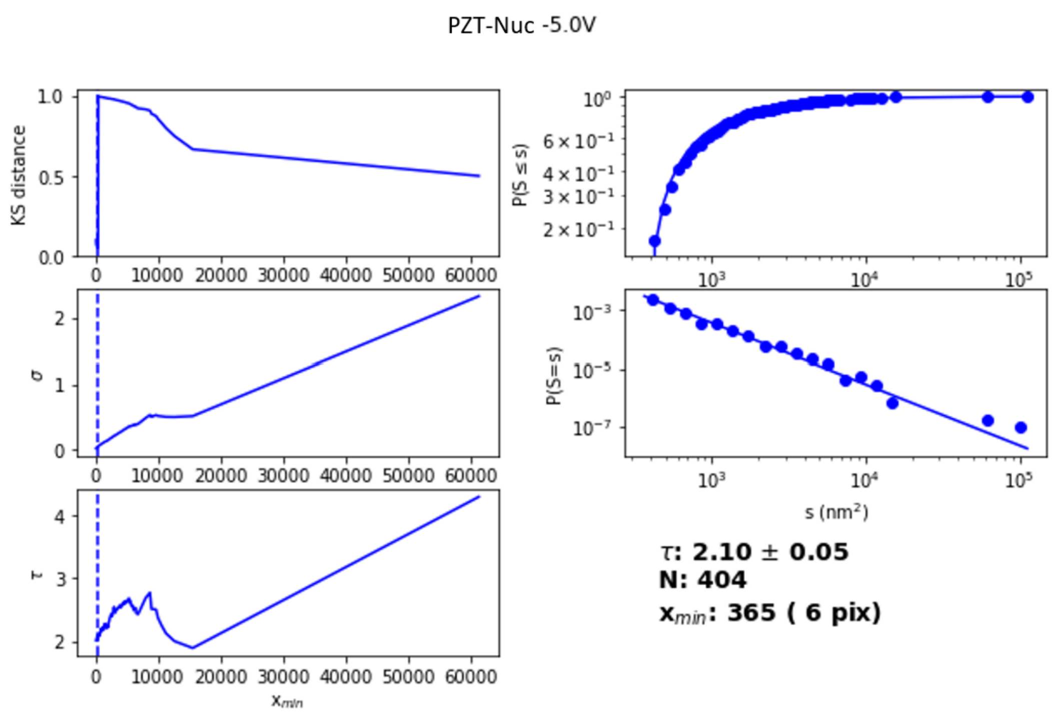

Figure 27. Power law fit characterization for the event sizes in PZT-Mot with a constant tip bias of -5.0 V. The blue dashed line shows the selected X_{min} value.

9 Switching dynamics at constant V_{tip}

Figure 28 shows the resulting maps of the local time required to reverse the polarization at individual pixels in units of the switching scan number. In the -3.5 V case, we observe only very slow switching dynamics. In particular, the pre-existing written domain walls appear to be strongly pinned in their initial positions, with only small displacements occurring in the first few switching scans where the domain walls are exploring more favorable configurations of the potential landscape in their immediate proximity, as shown in figure 28(a). We also observe very few nucleation events, occurring stochastically throughout the measurement series. The newly nucleated domains expand slowly under the applied tip bias as can be seen from close ups of some of the domains in figure 28(b). The stochastic nucleation of new domains throughout the measurement series, their ultraslow outward growth with time and the rapidly saturating growth of the initially written domain walls qualitatively suggest that the growth is occurring in the creep regime [1].

At a higher tip bias of -5V, the polarization reversal is much more rapid and polarization reversal events are much larger, although some down-oriented domains remain by the end of the measurement as seen by the white areas in the middle of figure 28(c).

[1] It is tempting to compare the values of the tip bias in the constant bias measurements shown here and in the measurements shown earlier where the tip bias is increased incrementally. However, these measurements were performed with separate tips which can lead to changes in the effective field applied to the sample. Moreover, the adsorbates at the surface of the sample can accumulate at the tip, further affecting the effective tip field significantly. Direct comparisons of switching dynamics at a given voltage between measurement series are therefore difficult, though within a given measurement series, the effective tip field usually does not appear to change significantly.

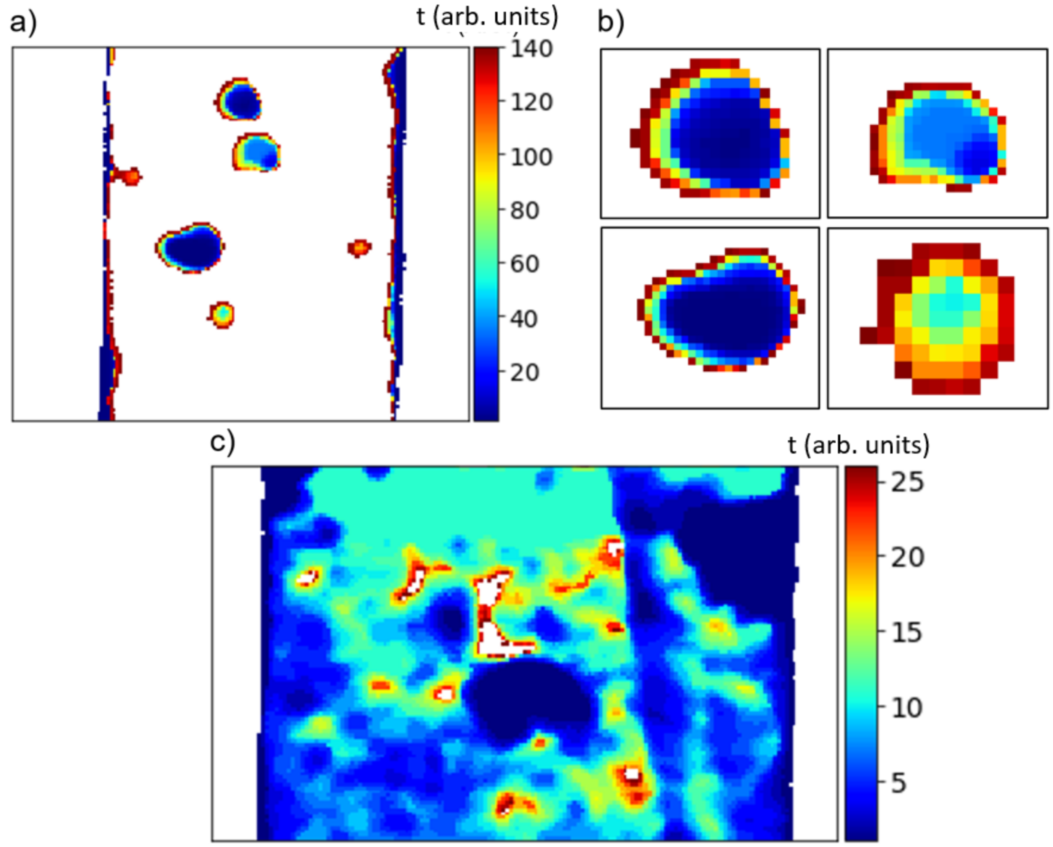

Figure 28. Switching time maps of initially written domains at constant tip bias. The time is expressed units of the number of switching scans. (a) $V_{tip} = -3.5$ V. Very limited switching occurs. The walls of the initially written domains move mostly only during the first applications of external tip bias. (b) The nucleation of new domains appears stochastically throughout the measurement series. (c) $V_{tip} = -3.5$ V. The switching dynamics is much more rapid with large events occurring throughout the measurement and rapid complete switching of the written domain.

10 Spatial distribution of switching events

The spatial distribution of events was analysed for the measurement on PZT-Nuc with $V_{tip} > 0$. The following figures (Figure 29 – Figure 31) show on the left the switching events corresponding to the inward domain wall motion (before nucleation and rapid merging). The estimated lower bound to the depinning force is 3.76 V. The panel on the right shows on the vertical axis, a (horizontal) line by line breakdown of the switching events. The events in the Nth line of the left panel correspond to the events in the Nth line of the right panel. The horizontal axis shows the bias at which the switching event occurred. The color code corresponds to the horizontal extent of the switching event. The plots suggest spatial clustering of switching events deep in the creep regime, with a gradual broadening of the event clusters as the tip bias is increased. For tip bias greater than 3.0 V, switching events are observed throughout the interface length.

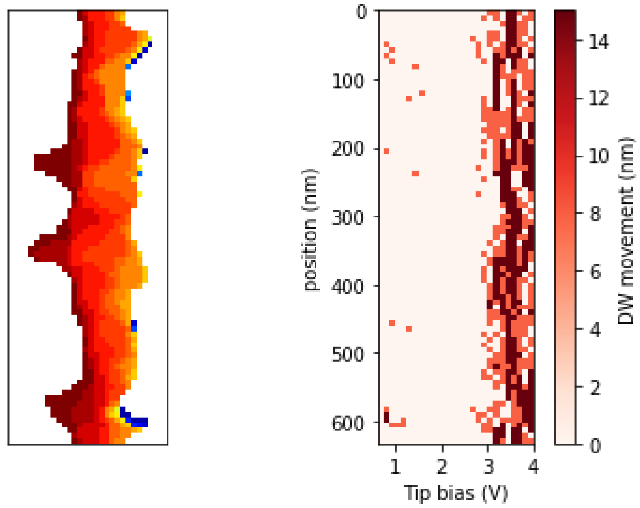

Figure 29. Left: Map of switching events along a moving domain wall in PZT-Nuc when the positive DC tip bias during switching scans is incrementally increased at each scan. Right: Map of the position of switched pixels along the vertical axis in the left panel as a function of the applied tip bias. The color code represents the depth (along the horizontal axis) of the switching event at that scan line. The map shows spatial correlation of events at low bias which breaks down as the switching bias is increased.

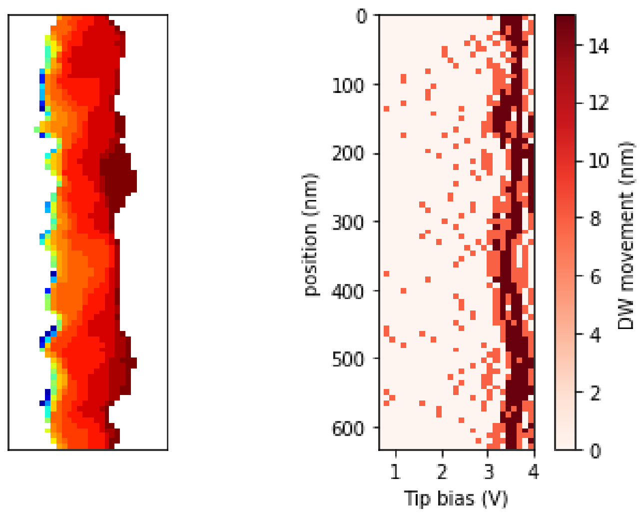

Figure 30. Left: Map of switching events along a moving domain wall in PZT-Nuc when the positive DC tip bias during switching scans is incrementally increased at each scan. Right: Map of the position of switched pixels along the vertical axis in the left panel as a function of the applied tip bias.

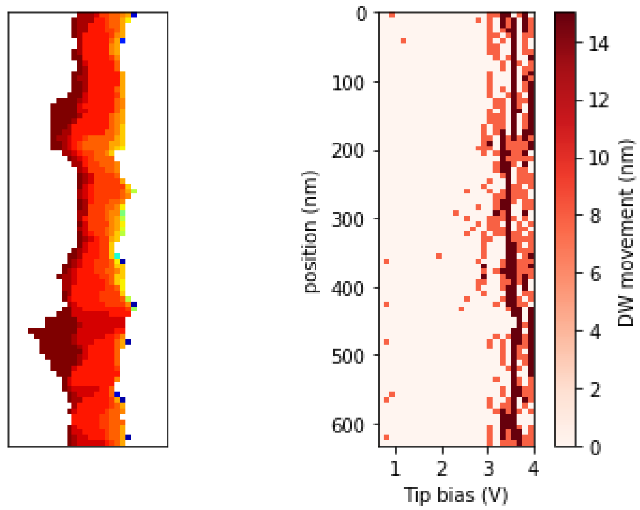

Figure 31. Left: Map of switching events along a moving domain wall in PZT-Nuc when the positive DC tip bias during switching scans is incrementally increased at each scan. Right: Map of the position of switched pixels along the vertical axis in the left panel as a function of the applied tip bias.

References

1. Ferrero, E. E., Bustingorry, S., Kolton, A. B. & Rosso, A. Numerical approaches on driven elastic interfaces in random media. *Comptes Rendus Physique* **14**, 641–650 (2013). URL http://dx.doi.org/10.1016/j.crhy.2013.08.002. 1304.0119.

2. Puppin, E. Statistical properties of barkhausen noise in thin Fe Films. *Physical Review Letters* **84**, 5415–5418 (2000).

3. Kim, D. H., Choe, S. B. & Shin, S. C. Direct Observation of Barkhausen Avalanche in CoThin Films. *Physical Review Letters* **90** (2003).

4. Grassi, M. P. *et al.* Intermittent collective dynamics of domain walls in the creep regime. *Physical Review B* **98**, 1–10 (2018).

5. Durin, G. & Zapperi, S. The barkhausen effect. In *The Science of Hysteresis*, vol. 2, 181–267 (2006). 0404512.

6. Salje, E. K. H., Xue, D., Ding, X., Dahmen, K. A. & Scott, J. F. Ferroelectric switching and scale invariant avalanches in BaTiO3. *Physical Review Materials* **3**, 1–8 (2019).

7. Le Doussal, P., Middleton, A. A. & Wiese, K. J. Statistics of static avalanches in a random pinning landscape. *Physical Review E - Statistical, Nonlinear, and Soft Matter Physics* **79**, 3–6 (2009).

8. Rosso, A., Le Doussal, P. & Wiese, K. J. Avalanche-size distribution at the depinning transition: A numerical test of the theory. *Physical Review B - Condensed Matter and Materials Physics* **80**, 1–12 (2009). 0904.1123.

9. Ferrero, E. E., Foini, L., Giamarchi, T., Kolton, A. B. & Rosso, A. Spatiotemporal Patterns in Ultraslow Domain Wall Creep Dynamics. *Physical Review Letters* **118**, 1–6 (2017).

10. Nattermann, T., Shapir, Y. & Vilfan, I. Interface pinning and dynamics in random systems. *Physical Review B* **42**, 8577–8586 (1990).

11. Chauve, P., Giamarchi, T. & Le Doussal, P. Creep and depinning in disordered media. *Physical Review B* **62**, 6241–6267 (2000).

12. Rosso, A., Hartmann, A. K. & Krauth, W. Depinning of elastic manifolds. *Physical Review E - Statistical Physics, Plasmas, Fluids, and Related Interdisciplinary Topics* **67**, 4 (2003). 0207288.

13. Giamarchi, T., Kolton, A. B. & Rosso, A. Dynamics of disordered elastic systems. In *Jamming, yielding, and irreversible deformation in condensed matter*, 91–108 (Springer, Berlin, 2006). 0503437.

14. Ferrero, E. E., Foini, L., Giamarchi, T., Kolton, A. B. & Rosso, A. Creep motion of elastic interfaces driven in a disordered landscape. *Arxiv* (2020). URL http://arxiv.org/abs/2001.11464. 2001.11464.

15. Sethna, J. P. Crackling noise and avalanches: scaling, critical phenomena and the renormalization group. In Bouchaud, J. P., Mezard, M. & Dalibard, J. (eds.) *Les Houches Summer School Proceedings*, vol. 85, 257–288 (Elsevier, Amsterdam, 2007).

16. Salje, E. K. & Dahmen, K. A. Crackling Noise in Disordered Materials. *Annual Review of Condensed Matter Physics* **5**, 233–254 (2014). URL http://www.annualreviews.org/doi/10.1146/annurev-conmatphys-031113-133838.

17. Pandya, S. *et al.* Strain-induced growth instability and nanoscale surface patterning in perovskite thin films. *Scientific Reports* **6**, 26075 (2016).

18. Gao, P. *et al.* Revealing the role of defects in ferroelectric switching with atomic resolution. *Nature Communications* **2**, 591–596 (2011). URL http://dx.doi.org/10.1038/ncomms1600.

19. Lee, J. K. *et al.* Direct observation of asymmetric domain wall motion in a ferroelectric capacitor. *Acta Materialia* **61**, 6765–6777 (2013). URL http://dx.doi.org/10.1016/j.actamat.2013.07.051.

20. Maksymovych, P. *et al.* Scaling and disorder analysis of local I-V curves from ferroelectric thin films of lead zirconate titanate. *Nanotechnology* **22**, 0–11 (2011).

21. Kalinin, S. V., Jesse, S., Tselev, A., Baddorf, A. P. & Balke, N. The Role of Electrochemical Phenomena in Scanning Probe Microscopy of Ferroelectric Thin Films. *ACS Nano* **5**, 5683–5691 (2011).

22. Ievlev, A. V. *et al.* Chemical Phenomena of Atomic Force Microscopy Scanning. *Analytical Chemistry* **90**, 3475–3481 (2018). URL https://pubs.acs.org/doi/10.1021/acs.analchem.7b05225.

23. Ievlev, A. V. *et al.* Nanoscale Electrochemical Phenomena of Polarization Switching in Ferroelectrics. *ACS Applied Materials and Interfaces* **10**, 38217–38222 (2018).

24. Ievlev, A. V. *et al.* Non-conventional mechanism of ferroelectric fatigue via cation migration. *Nature Communications* **10**, 1–8. URL http://dx.doi.org/10.1038/s41467-019-11089-w.

25. Domingo, N. *et al.* Surface charged species and electrochemistry of ferroelectric thin films. *Nanoscale* **11**, 17920–17930 (2019).

26. Jesse, S., Baddorf, A. P. & Kalinin, S. V. Switching spectroscopy piezoresponse force microscopy of ferroelectric materials. *Applied Physics Letters* **88**, 1–4 (2006).

27. Miller, R. C. & Weinreich, G. Mechanism for the Sidewise Motion of 180 Domain Walls. *Physical Review* **117**, 1460–1466 (1960).

28. Alstott, J., Bullmore, E. & Plenz, D. Powerlaw: A python package for analysis of heavy-tailed distributions. *Public Library of Open Science One* **9**, 1–18 (2014).

29. Clauset, A., Shalizi, C. & Newman, M. Power law distributions in empirical data. *Society for Industrial and Applied Mathematics Review* **51**, 661–703 (2009).

30. Tybell, T., Paruch, P., Giamarchi, T. & Triscone, J.-M. Domain Wall Creep in Epitaxial Ferroelectric Pb(Zr0.2Ti0.8)O3 thin films. *Physical Review Letters* **89**, 097601 (2002). URL https://link.aps.org/doi/10.1103/PhysRevLett.89.097601.